Map-Based Channel Model for Evaluation of 5G Wireless Communication Systems

Pekka Kyösti, Janne Lehtomäki, *Member, IEEE,* Jonas Medbo, and Matti Latva-aho *Senior Member, IEEE*

***Abstract*—This paper presents a channel model for the fifth generation (5G) air interface evaluations. The described model covers frequency bands from typical cellular frequencies up to millimetre waves and a variety of different environments, with emphasis on the urban outdoor. The model enables assessment of single radio links with, e.g., the massive multiple-input-multiple-output (MIMO) and very large antenna arrays, device-to-device (D2D) links with both link ends moving, up to system level evaluations with a multitude of different types of transceivers. In addition to the overview some selected model features are described in more detail. Also few exemplary model outputs are depicted and discussed. A comparison to corresponding geometry based stochastic model (GSCM) is performed in urban outdoor environment with the second moment distributions of propagation parameters and with the multi-user (MU) MIMO sum rate capacity. The simulations indicate substantial differences in MU-MIMO performances between the models.**

***Index Terms*—Propagation, MIMO systems, ray tracing.**

I. Introduction

Active research, standardization, and also development on 5G systems is ongoing in the telecommunication area currently. The systems are requested to serve at least higher data rates in mobile broadband, ultra reliable and low latency transmission, e.g., for autonomous car, car-to-car, and car-to-infrastructure communications, and massive machine type communications with numerous transceivers [1], [2]. The coming 5G wireless communication systems are expected to contain various different link types. The size of cells may decrease; traditional macro- and micro-cells are going to be complemented by pico- and femto-cells composing ultra-dense networks, moving base stations and peer-to-peer type of D2D connections between user terminals [2]. These various types of links will co-exist in the same area. The number of communicating devices and thus the density of the radio links is is going to grow significantly [1]. The utilized frequency bands may have a wide range from below one GHz up to 100 GHz [3]. New antenna topologies, like massive MIMO with tens or hundreds of closely packed elements, and very large arrays with possibly physical dimensions of tens of meters, may be used [1].

The above mentioned features set new requirements to channel modelling, as discussed in [4]–[6] and also in [3]. The four main demands identified are; spatial consistency and mobility, diffuse vs. specular scattering, very large antenna arrays, and millimetre wave frequencies. Especially the last requirement has drawn many contributions on measurements and channel modelling, recent activity is summarized, e.g., in [7] and [8]. ITU-R has identified that even 2 GHz of bandwidth is needed to address the increase of data traffic [9]. The bandwidth is not available on the current cellular frequencies, thus a new frequency spectrum, including mm-frequencies, is required for 5G.

A different challenge for channel modelling is the wide range of simulation needs [10]. On one extreme a very precise modelling of propagation phenomena is required in order to evaluate, e.g., the gains of large antenna systems. Spherical wave modelling is useful in order to treat the combination of physically large arrays, small wavelengths, and dense networks indicating short link distances. Assessment of antenna designs will require realistic modelling of depolarization of the propagation channel. Large arrays have a very high angular resolution. Wide bandwidths, available on mm-frequencies, provide high delay resolution. This will require reconsideration of the widely adopted cluster concept. Now sub-paths within a cluster may become resolvable and the structure of a cluster has to be defined more carefully.

Further, the target is to model the received power level, determined by the path loss and shadowing, accurately enough for system level simulations. As identified in simulation guidelines of METIS project [11], for the sake of inter-link consistency it is preferred to base the path loss and shadowing determination on a geometrical environment description instead of mere distance and line-of-sight (LOS) probability as was the case in 4G channel models defined in [12], [13]. In order to get reliable and comparable results the evaluation of 5G communication systems is preferably performed with a single, but scalable, channel model. Thus the channel model should be consistent across a wide range of environments, network topologies, and frequencies. Our purpose is to give a complete but compact description of the proposed model. For completeness we chose to give the final mathematical formulas for each step of the model, even in the cases they may be well known.

Channel model requirements are discussed in detail in section II together with the existing models. In section III we describe the channel model proposal. An overview description is given in [10] and here we focus on the mathematical

P. Kyösti is with Centre for Wireless Communications (CWC), University of Oulu, Oulu, FI-90014 Finland (email: pekka.kyosti@oulu.fi) and Keysight Technologies Finland Oy, Oulu, Finland.

J. Lehtomäki and M. Latva-aho are with Centre for Wireless Communications (CWC), University of Oulu, Oulu, FI-90014 Finland (email: firstname.lastname@oulu.fi).

J. Medbo is with Ericsson Research, Ericsson AB, 164 80 Stockholm, Sweden (e-mail: jonas.medbo@ericsson.com).

formulation[1] at sufficient level of details to compose all model features together. On background information, e.g., of determining physical interaction coefficients, we mostly refer to [4] and the original references. We discuss validation of the proposed model in section IV. In section V a computer program is used to generate realizations of the proposed model, which are then analyzed and compared to outputs of a GSCM. The emphasis of the comparison is on the spatial inter-link characteristics and their impact on the MU-MIMO sum rate capacity. A summary and discussion on model improvements is given in section VI.

II. Existing models and channel model requirements

A. Existing models

The main stream in spatial channel modelling has been on GSCMs. They model spatial radio channel with randomly drawn directional and other propagation parameters, without any particular definition of the environment in form of, e.g., maps or layouts in a coordinate system. Jaeckel et al. [6] gives clear overview on 3D state-of-the-art GSCMs and reflects their capabilities with respect to the new requirements. To the line of considered models must be added the recently specified 3GPP channel model for above 6 GHz frequencies [8]. There the previous 3GPP 3D model [14] is updated to higher frequency bands. The updates concern mainly parameterizations, with emphasis on the path loss modelling. However, some new optional features are introduced to address the other requirements. A statistical spatial channel model for 5G is introduced in [7], which directly utilizing mm-wave measurements extends the current 3GPP model with the so called time cluster and spatial lobe features.

It is worth mentioning that [8] specifies also an alternative model to the GSCM, called the hybrid model. The hybrid model is a combination of deterministic and stochastic modelling principles, of which the former component can be implemented, e.g., by the map-based model introduced in this paper.

B. Channel model requirements

1) Spatial consistency and mobility: requires that all channel characteristics are geometry specific and vary continuously as either end (or both ends) of the radio link is (are) moving. Utilizing the ray tracing principles all propagation parameters are precisely dependent on transmitter/receiver locations with respect to the environment. Smaller or larger motion resulting to a displacement of transceivers is accounted for when determining propagation characteristics like, e.g., path loss, shadowing or angular parameters. Also the possible motion of both link ends, which is an important feature in vehicular and D2D communications, is implicitly modelled by the ray tracing principles. The coordinate based deterministic approach enables consistency with respect to all possible transceiver location combinations on the 3D map. Full consistency is very difficult to achieve with traditional GSCMs like [12], [13] where neither cluster locations nor visibility regions are defined.

2) Diffuse vs. specular scattering: i.e. scattering caused by rough materials and small objects vs. large smooth surfaces, results in substantially different propagation channel characteristics. The diffuse component of the channel is typically rich and spread out in direction whereas the specular component is composed of a few spikes in direction and delay. In the proposed model the diffuse part is handled by dividing larger surfaces into tiles, as proposed in [15]. For the specular scattering straight forward ray-tracing is used in modelling the corresponding paths reflected from smooth surfaces like, e.g., walls. The specular paths, determined utilizing ray optics principles, will be non-fading and their departure and arrival directions will change consistently while the link ends are moving. Thus in a performance simulation with, e.g. high angular resolution antenna arrays, the transmitter/receiver has to track realistically moving specular paths. GSCM may model the diffuse tail of propagation paths by introducing appropriate sub-paths around dominant components, but modelling of realistic specular paths is not possible, when the environment is not geometrically defined.

3) Very large antenna arrays: i.e. arrays which are very large in terms of the number of elements or size in terms of the number of wavelengths. Optimization of such large arrays is crucially dependent on accurate and realistic modelling of highly resolved directional channel characteristics. Very large arrays, considered in METIS project [2] and in [16], may experience non-stationary propagation channel with variation of large scale effects like shadow fading across the array. The assumption of a confined physical size to antenna arrays, a prerequisite in the existing GSCMs [12], has to be given up. The proposed model, being based on a map with coordinates, supports determination of propagation channels between any locations, thus there is no need to assume a confined physical size for antenna arrays. Further, the proposed model supports spherical waves inherently. Each interaction point and antenna element has coordinates, and both the phase and attenuation are affected by Euclidean distances between interaction points and antenna elements.

4) Millimetre wave frequencies: down to sub-GHz frequencies for 5G evaluations have to be preferably modelled consistently across the wide frequency range. As defined in [4] and in [8] the existing empirical path loss models like, e.g., [13] can be extended to millimetre waves. Further, it is possible to parameterize the existing GSCMs for discrete frequency bands as is done in [4], [17], e.g., for the shopping mall scenario at 60 GHz. The stochastic model of [8] introduces a frequency dependent component for the distribution parameters of angular and delay spreads. In the proposed map-based model, different radio channel characteristics are smoothly reconstructed while the model is based on frequency dependent propagation mechanisms like reflection and diffraction. As an additional frequency dependent effect, the surface roughness may be accounted for as a function of wavelength.

[1]The model (METIS map-based model) was presented in technical report [4, Section 6] and in EuCAP [5]. We extend these earlier materials by including validation part, new simulation results, and some corrections and amendments to the description of [4].

C. Computational complexity

All modelling in general has to balance between accuracy and complexity. One of the main concerns, e.g. in 3GPP, on map-based modelling has been the computational complexity related to the generation of model outputs. An implementation for the so called map-based hybrid model was done by ZTE during the process of specifying [8] in 3GPP. The deterministic part of the implemented model is on conceptual level similar to the proposed model of this paper. In [18] is shown that 1) the computing time of the deterministic model is linearly dependent on the number of Tx and Rx, 2) the more transceivers are to be modelled the closer to the GSCM computing times are achieved, and 3) the overall time consumption is well acceptable for the system level evaluations. Relying on these observations we conclude that with a sophisticated implementation the computational complexity should not prevent utilization of deterministic modelling even for system simulations.

III. Channel Model Description

The proposed model is based on the ray tracing using a simplified 3D geometric description of the propagation environment and deterministic modelling of propagation in terms of rays. Building walls are modelled as rectangular surfaces with specific electromagnetic material properties. The significant propagation mechanisms i.e. diffraction, specular reflection, diffuse scattering, blocking etc. are accounted for. For each specific link between Tx and Rx there are a number of pathways which contribute significantly to the received power.

A block diagram of the channel model is illustrated in Fig. 1 with numbered steps of the procedure to generate radio channel realizations. On higher level the procedure is divided to four main operations: creation of the environment, determination of propagation pathways, determination of propagation channel matrices for path segments, and composition of the radio channel transfer function. In the following we describe the main operations briefly. The overall procedure is functionally similar to the ray tracing approach described in [19].

A. Creation of Environment

The first four steps in Fig. 1 are for creating the environment. As a starting point a 3D geometric description is required. The map contains coordinate points of wall corners where walls are modelled as rectangular surfaces as mentioned earlier. Secondly, a set of random scattering/shadowing objects, representing humans, vehicles, etc., is drawn on the map with a given scenario dependent density. The role of objects is discussed with more details in the next section. Thirdly, the surfaces, like walls, are divided to tiles with certain tile centre coordinate points for diffuse scattering modelling. After these three steps the environment is defined. In the step number four transceiver locations or trajectories are defined. It is also possible to draw the transceiver locations randomly which is analogous to the drop simulations of GSCMs.

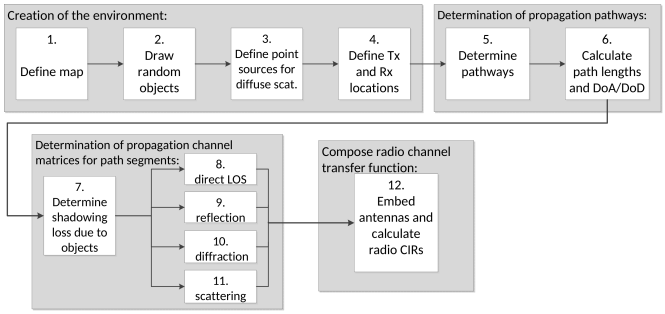

Fig. 1. Block diagram of map-based model.

B. Determination of Pathways

The next operation is to determine propagation pathways from transmitter to receiver in the environment specified in the previous steps. The search is started from the Tx or Rx location and all possible second nodes visible to the Tx / Rx node either with a LOS path or via a single specular reflection are identified. Possible second nodes are diffraction points like corners, scattering objects or diffuse scattering point sources. Further, specular images are also considered as second nodes in this step. Then the coordinates and interaction types of interaction points (diffraction nodes and specular reflection points) are determined. Possible pathways are identified by checking whether any wall is blocking the direct or single order reflected paths. The procedure described in [19], [20] or [21] can be followed. For specular image nodes, blocking occurs also if the path does not intersect the corresponding reflection surface. This procedure may be repeated to achieve any number of diffraction and specular reflection interactions. When repeated, the nodes of previous steps act as Tx / Rx of the first step. Only single order diffuse scattering is considered in the path discovery, due to strong attenuation in the propagation mechanism [20].

In the step five the pathways are defined for given transmitter and receiver antenna elements u and s, respectively, by a set of parameter vectors $\mathbf{\Psi}_k = \{\Psi_{ki}\} = \{x_{ki}, y_{ki}, z_{ki}, T_{ki}\}, k = 1, \ldots, K, i = 0, \ldots, I_k$, where K is the number of pathways, I_k is the number of path segments, x_{ki}, y_{ki}, z_{ki} are x, y and z coordinates of ith interaction point of kth pathway, and T_{ki} is the interaction type {direct, reflection, diffraction, object scattering, diffuse scattering}. It is defined that Ψ_{k0} denotes Rx and Ψ_{kI_k} denotes Tx and T_{kI_k} is always of type LOS. Coordinates of interaction points for parameter vectors are determined utilizing mathematical tools of analytical geometry. After the pathways are determined the corresponding path lengths and arrival and departure directions are calculated. The mentioned directions are used in the very last step as arguments to radiation patterns of Tx and Rx antennas.

C. Determination of Propagation Matrices

Propagation matrices are determined for path segments and corresponding interactions. A propagation matrix is complex 2×2 matrix describing gains of polarization components in the interaction. Phases and amplitudes based on path length,

wavelength and the free space loss including spreading are accounted for in the section III-D. For example for the line-of-sight path the matrix is a diagonal matrix with unity gains. With specular reflection the matrix is determined based on well-known Fresnel reflection coefficients, and in the case of diffraction the matrix is calculated using the uniform theory of diffraction (UTD). Alternatively diffraction may be determined with an approximation method originally defined by Berg in [22]. Scattering may occur either from a random object or as a diffuse scattering from a tile of wall or other environment surfaces. For diffuse scattering the gains are calculated similarly to [15]. In the case of object scattering the gains are based on the scattering cross section of the object.

Jones calculus [23] can be used to describe wave polarization. Radiation patterns of transmitter and receiver antenna elements are composed of Jones vectors, where the polarization state is defined by two polarization components. The mentioned 2×2 propagation matrices are used in Jones calculus to determine the depolarization along the pathway. Geometrical depolarization occurs in reflections if the reflective surface is tilted with respect to the reflection plane. Diffraction does not cause depolarization of waves. In the following the depolarization due to scattering is modelled as random. The actual Jones calculus is described in section III-D.

Determination of propagation matrices for the mentioned interaction types is briefly introduced in the following subsections. Details are given in [4] and in the cited original papers. The polarization matrix for a particular interaction

$$\mathbf{h} = \begin{bmatrix} \alpha_{\theta\theta} & \alpha_{\theta\phi} \\ \alpha_{\phi\theta} & \alpha_{\phi\phi} \end{bmatrix} \in \mathbb{C}^{2\times 2} \tag{1}$$

defines co- and cross-polarized transmission coefficients for the incident θ and ϕ polarizations. Also divergence factors for different interaction types are given. The divergence factor describes the spreading of a wave as a function of distance [15].

1) Direct line-of-sight: With LOS path segments the polarization is not changing and the power attenuation is proportional to the distance squared. Thus the propagation transfer matrix for ith segment of kth path from Tx element s to Rx element u is given by

$$\mathbf{h}^{\mathrm{los}}_{k,i,u,s} = \begin{bmatrix} 1 & 0 \\ 0 & -1 \end{bmatrix} \tag{2}$$

and the divergence factor is

$$F^{\mathrm{los}}_{k,i,u,s} = 1/s_{in}, \tag{3}$$

where s_{in} is the length of the LOS path segment from Tx to the next node in metres. The divergence factor of LOS path is applied in eq. (17) only for the path segment from Tx to the next node. It is assumed that signals propagate to all directions from the transmitter and the propagation direction is not changed in LOS path segments. Of course finally the effect of antenna radiation patterns is taken into account in section III-D.

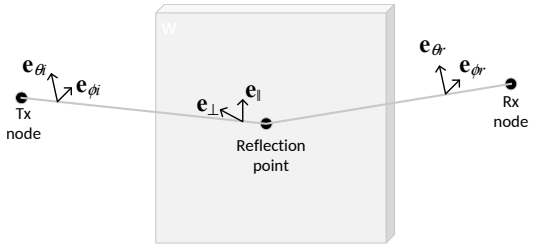

Fig. 2. Definition of unit vectors in reflection.

2) Reflection: Specular reflections are possible from wall surfaces and the ground, in indoor cases also from floor and ceiling. Reflections are determined utilizing the principles of geometrical optics. An incident ray reflects only to a certain direction according to the Snell's law. The propagation transfer matrix is

$$\mathbf{h}^{\mathrm{ref}}_{k,i,u,s} = \beta \begin{bmatrix} \alpha_{\theta\theta} & \alpha_{\theta\phi} \\ \alpha_{\phi\theta} & \alpha_{\phi\phi} \end{bmatrix} \tag{4}$$

where β is the ratio of reflected and scattered power (a model parameter), elements of the polarization matrix are defined as

$$\alpha_{ab} = (\mathbf{e}_{ar} \cdot \mathbf{e}_{\perp r})(\mathbf{e}_{bi} \cdot \mathbf{e}_{\perp i} R_{\perp}) + (\mathbf{e}_{ar} \cdot \mathbf{e}_{\parallel r})(\mathbf{e}_{bi} \cdot \mathbf{e}_{\parallel i} R_{\parallel}) \tag{5}$$

where $a, b \in \{\theta, \phi\}$, unit vectors $\mathbf{e}$ are described in Fig. 2, and $R_{\perp}, R_{\parallel}$ are the Fresnel reflection coefficient as specified in [4], [24]. Geometrical depolarization is accounted for by means of the Jones calculus. The matrix $\mathbf{h}^{\mathrm{ref}}$ is a Jones matrix, where entries defined by eq. (5) introduce rotations by dot products of unit vectors. Alternatively to eq. (4) and (5) reflection coefficients can be determined with a recursive method for multi-layered surfaces as described in [25]. This would be beneficial if, e.g., windows or other layered surfaces would be liked to be modelled carefully. The divergence factor for reflection is

$$F^{\mathrm{ref}}_{k,i,u,s} = \frac{s_r}{(s_{in} + s_r)}, \tag{6}$$

where s_{in} is the cumulative distance from Tx to the reflection point and s_r is the distance from the reflection point to the next node.

3) Diffraction: Edges of building corners and roof tops can be approximated as wedges. A ray, diffracted from a wedge, propagates along the surface of a Keller's cone [26] as illustrated in Fig. 3. The propagation transfer matrix is

$$\mathbf{h}^{\mathrm{dif}}_{k,i,u,s} = \begin{bmatrix} D_a & D_b \\ D_c & D_d \end{bmatrix}. \tag{7}$$

The proposed model provides two options for modelling of diffraction. The first option is based on the uniform theory of diffraction (UTD) and provides more accurate modelling. Despite its complexity UTD was chosen for diffraction modelling instead of, e.g., the knife edge diffraction, because it contains frequency dependent material parameters and the polarization consideration. Matrix entries are determined with UTD [26]

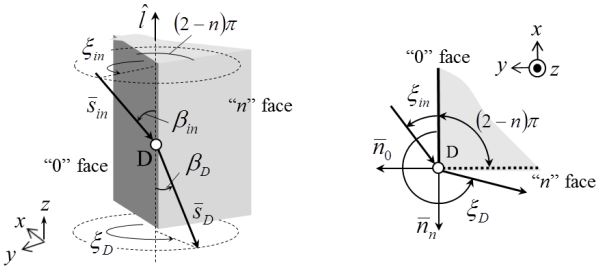

Fig. 3. Definition of incidence and diffraction vectors and angles in diffraction point D. (Reprinted from [4].)

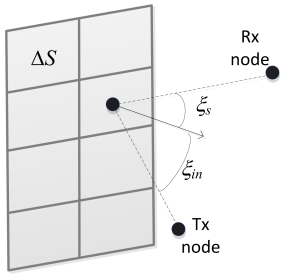

Fig. 4. A surface divided to tiles for diffuse scattering.

as detailed in [4], [27]. The incidence $\mathbf{e}_{\beta in}$, $\mathbf{e}_{\xi in}$ and the diffracted $\mathbf{e}_{\beta D}$, $\mathbf{e}_{\xi D}$ unit vectors for θ and ϕ polarizations, respectively, are defined in [4] based on Fig. 3.

The divergence factor for UTD diffraction is

$$F^{\text{dif}}_{k,i,u,s} = \sqrt{\frac{s_{in}}{s_D(s_{in}+s_D)}} \tag{8}$$

where s_{in} is the cumulative distance from Tx to the diffraction point and s_D is the distance from the diffraction point to the next node. A drawback with the UTD approach is, however, it results to high complexity. An alternative method to determine diffraction, together with the other propagation mechanisms, is to use Berg's recursive model as described in [4], [22]. The Berg recursive model is semi-empirical and designed for signal strength prediction along streets in an urban environment. It is semi-empirical in the sense that it reflects physical propagation mechanisms without being strictly based on electro-magnetics theory. It is based on the assumption that a street corner appears like a source of its own when a propagating radio wave turns around it.

4) Diffuse scattering: The propagation matrix for scattering is

$$\mathbf{h}^{\text{sc}}_{k,i,u,s} = \sqrt{G^{\text{sc}}_{k,i,u,s}} \begin{bmatrix} e^{j\Phi^{\theta\theta}_{k,i}} & e^{j\Phi^{\theta\phi}_{k,i}} \\ e^{j\Phi^{\phi\theta}_{k,i}} & e^{j\Phi^{\phi\phi}_{k,i}} \end{bmatrix} \tag{9}$$

where G^{sc} is a gain term. Phase terms $\Phi^{ab} \sim \text{Uni}(0, 2\pi)$, $a, b \in \{\theta, \phi\}$ are modelled as uniformly distributed random variables due to surface roughness, which results to random elliptical polarization. The divergence factor for scattering is

$$F^{\text{sc}}_{k,i,u,s} = 1/s_s \tag{10}$$

where s_s is the distance from the scattering point to the receiver node. Diffuse scattering may occur from the same surfaces as specular reflection like walls etc. In the model waves are scattered to all directions in the half space defined by the surface, regardless of the incidence angle. Surfaces can be divided to rectangular tiles whose centres may act as scattering points. Also a random distribution of scattering points on the surface can be used. The gain for diffuse scattering [4], [15]

$$G^{\text{sc}} = \frac{\lambda^2 \Delta S(1-\beta)\cos\xi_{in}\cos\xi_s}{64\pi^3} \tag{11}$$

is dependent on the specular/diffuse power ratio β, area of the scattering tile ΔS, and the incidence and the scattering angles relative to the normal of the surface ξ_{in}, ξ_s, respectively, that are defined in Fig. 4.

5) Scattering by objects: Both the propagation matrix and the divergence factor are the same as in diffuse scattering. The scattering gain G^{sc} is defined differently for objects. Starting point for the derivation is the scattering cross section for a conductive sphere πR^2, where R is the radius. While objects are defined as rectangular screens with height h and width w (see Fig. 5) the cross section of a sphere is matched by setting $R = \sqrt{(wh/\pi)}$. With derivation as shown in [4], [28] the gain is $G^{\text{sc}'} = \left(\frac{\lambda R}{8\pi}\right)^2$. However, the scattered power is simultaneously shadowed as defined in III-C6, thus the final scattering gain of objects to be substituted to eq. (9) is

$$G^{\text{sc}} = \frac{1-\alpha}{L_{sh}} \left(\frac{\lambda R}{8\pi}\right)^2 \tag{12}$$

where α is the absorption coefficient of the object (model parameter) and the shadowing loss L_{sh} is defined by eq. (13). Scattered signal from an object propagates to all directions (full space), but the shadowing is heavily dependent on the incidence and scattering angles.

6) Shadowing by objects: Shadowing due to objects is calculated in the step seven for path segments having objects in the close vicinity. The effect of blocking may be significant, particularly for higher frequencies in the millimetre range. The shadowing is based on knife edge diffraction across a screen representing the object.

Each path may be obstructed by objects representing, e.g., humans or vehicles. This effect is accounted for using a simplified blocking model [28]. A blocking object is approximated by a rectangular screen as illustrated in Fig. 5. The screen is always perpendicularly oriented to any path it interacts with, i.e. with respect to the line connecting the two nodes of the link. If either or both nodes are moving the screen turns around its centre accordingly.

The shadowing loss is modelled using the following knife edge diffraction model for the four edges of the screen

$$L_o = \frac{1}{(1-(Z_{h1}+Z_{h2})(Z_{w1}+Z_{w2}))} \tag{13}$$

where $o = 1, 2, \ldots, O_{k,i,u,s}$ denotes the oth object on the path segment k, i between antennas u, s, and $Z_{h1}, Z_{h2}, Z_{w1}, Z_{w2}$

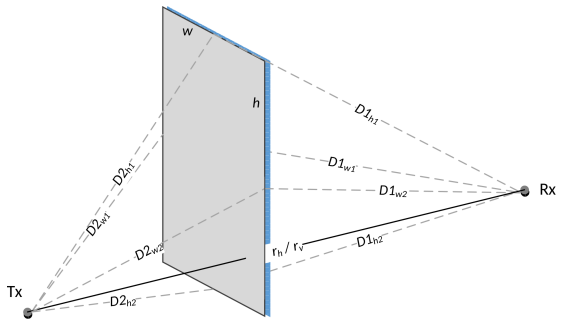

Fig. 5. Screen representing a shadowing object.

account for knife edge diffraction at the four edges. The diffraction terms are determined as

$$Z_{ab} = \frac{\arctan\left(\pm\frac{\pi}{2}\sqrt{\frac{\pi}{\lambda}(D_{1,ab} + D_{2,ab} - r_a)}\right)}{\pi} \tag{14}$$

where $a \in \{h, w\}$, $b \in \{1, 2\}$, λ is the wavelength, $D_{1,ab}$ and $D_{2,ab}$ are the first and the second projected distance between a screen edge and a node, respectively, and r_a is the projected distance between the nodes as illustrated in Fig. 5. The mentioned distances are defined as projections to a vertical or horizontal plane, i.e. as seen from either the side or the top. The sign of the argument in the inverse tangent of eq. (14) is defined as follows. If in a projection the screen is blocking LOS between Tx and Rx the signs are positive for both edges (shadow zone). If Tx and Rx have LOS in a projection the farthest edge has positive sign and the closest edge negative sign.

If there are several sparsely distributed objects shadowing the path segment k, i the total shadowing loss is the product of corresponding losses. However, if the objects (screens) are dense located the total loss may be over-estimated by the product. To avoid this the total shadowing loss is modified by a loss term determined by the Walfisch-Bertoni model [29]

$$Q = a\left(\theta\sqrt{d_{av}/\lambda}\right)^b \tag{15}$$

where d_{av} is the average inter-object distance on the path segment as projected to the line between the previous and the next node, θ is the incidence angle in radians, a and b are model constants. The original constants from [29] are updated to values $a = 1.4$ and $b = 0.976$ by a measurement [30] conducted at frequency band 10–18 GHz with varying number of metallic screens acting as obstacles.[2] Intention of the measurement was in particular to update this multiple screen shadowing term of the map-based model. For the cases where both link ends are at or below the level of top-most edges of shadowing objects the incidence angle is lower bounded. See illustrations and definition of θ in [4, Fig 6-4].

Finally the shadowing loss for the path segment is

$$L_{k,i,u,s} = \begin{cases} \prod_{o=1}^{O_{k,i,u,s}} L_o & \text{if } \theta\sqrt{d_{av}/\lambda} \geq 0.4 \\ Q\max(L_1, L_O) & \text{if } \theta\sqrt{d_{av}/\lambda} < 0.4, \textit{above} \\ QL_1L_O & \text{if } \theta\sqrt{d_{av}/\lambda} < 0.4, \textit{below} \end{cases} \tag{16}$$

where L_1 and L_O are the losses of the first and the last object counted from Tx, respectively. The sparsity of objects is proportional to the average inter-element distance in wavelengths and the incidence angle, "*above*" denotes the case where at least either node is above the objects and "*below*" where both nodes are below the level of top-most edges of objects.

For path segments with no blockage by objects $L = 1$. To reduce complexity only objects within the three first Fresnel zones [24, Appendix D] are considered. It is noted that the above defined loss term L is an amplitude value, not a power value (see its usage in eq. (17)). The introduced blockage model enables synthesizing arbitrary shaped objects by composing them with a number of rectangles.

D. Calculation of Radio Channel Transfer Functions

The last operation is to compose the radio channel transfer functions by embedding antenna radiation patterns to shadowing losses (from step 7) and composite propagation matrices. For a single path the complex gain is calculated as a product of the polarimetric antenna radiation pattern vectors, product[3] of propagation matrices of each path segment of the path, and the total shadowing loss.

The resulting transfer function contains all modelled antenna and propagation effects in the given environment for the specified Rx and Tx antenna locations

$$H_{u,s}(t,f) = \sum_{k=1}^{K} \mathbf{g}_u\left(-\mathbf{k}^{RX}_{k,u,s}(t)\right) \prod_{i=1}^{I_k}\left(\frac{\mathbf{h}_{k,i,u,s}(t)}{L_{k,i,u,s}(t)} F^{T_{ki}}_{k,i,u,s}(t)\right) \mathbf{g}_s\left(\mathbf{k}^{TX}_{k,u,s}(t)\right)^T \frac{\lambda}{4\pi} e^{j2\pi f \tau_{k,u,s}(t)} \tag{17}$$

where t is the time instant, $\mathbf{g}_u = \left[g^\theta_u\, g^\phi_u\right]$ and $\mathbf{g}_s = \left[g^\theta_s\, g^\phi_s\right]$ are the complex polarimetric antenna gain vectors of θ and ϕ polarizations for Rx antenna element u and Tx antenna element s, respectively. Further, wave vectors $\mathbf{k}^{RX}_{k,u,s}$ and $\mathbf{k}^{TX}_{k,u,s}$ define both the frequency and the direction of arrival/departure to sample the radiation patterns of Rx/Tx antennas, $d_{k,u,s}$ is the total length of the path k from element s to element u, $\tau_{k,u,s} = d_{k,u,s}/c$ is the total path delay, $\lambda = c/f$ is the wavelength, and c is the speed of light.

It is noted that the term $\frac{\lambda}{4\pi}$ is missing from [4, Sect 6.2 step 12], it is supplemented here to take into account the power density of transmitted field and the effective antenna cross section of the Rx antenna. The product of divergence factors contains always the the first segment of LOS type. For example a path with single reflection has the divergence factor term as the product of F^{los} for the distance s_{in} from Tx to the

[2]Note: the original values $a = 2.35$ and $b = 0.9$ were used in [4] as well as in the simulation section V.

[3]Note: this is a normal matrix product, despite [4] defines it mistakenly as a element-wise matrix product. For reasoning, see [24, Sect 6.7.2.1] or [23].

reflection point and F^{ref} with the distances s_{in} and s_r, where the latter is from the reflection point to Rx.

The transfer function of eq. (17) has time variability due to true motion of Tx, Rx, or the environment. Wave vectors indicating arrival and departure angles, as well as propagation matrices and shadowing losses are time variant in the case of motion. Alternatively small scale fading can be modelled with the so called virtual motion. This is the method of GSCMs to generate the small scale fading [12, Section 3.4]. There the propagation parameters are kept constant and only the phases of individual path coefficients are rotated based on Doppler shifts ω_k^D. The sum contribution of paths results to a temporal fading and a Doppler power spectrum. Eq. (17) can be modified to support the virtual motion by introducing a new phasor term $e^{jt\omega_k^D}$ to the summation over K and by removing the time argument t from the other terms.

IV. Validation

Validation of any developed channel model is important [19]. By validation is often meant a successful comparison of model outputs, i.e. channel parameters or statistics generated by the model, with the real world radio channels. The latter information is typically obtained by radio channel measurements. A thorough comparison across all different environments, frequencies, transceiver deployment scenarios/network topologies, transceiver mobility scenarios, and antenna array alternatives would require a huge effort. This cannot be necessarily done, partially because of the effort required, but mainly because such an inclusive measurement data set is not available. However, we may get fair confidence to the model by validating its building blocks by site-specific measurements and relying on that if the basic mechanisms are modelled properly the overall model is adequate in a wide range of conditions [19]. In the following, we introduce briefly two measurements validating the model components in specific sites and a third measurement comparing statistics of extracted and predicted path losses.

A. Indoor

An indoor measurement at 28–30 GHz frequency, with the purpose to validate the map-based model, is described in [31]. The measurement was performed with a vector network analyzer, a biconical antenna at Tx, and a horn, rotated full azimuth sweep of 360°, at Rx. The environment was a large room opening to a corridor. Dominant paths trajectories and powers were compared in three scenarios: LOS, NLOS, and obstructed LOS (OLOS). The OLOS condition was obtained placing a white board to shadow the LOS path. A layout identical to the measurement site was defined for the map-based model.

In LOS case the direct path and four reflected paths were dominant. Path trajectories were predicted correctly by the model as well as powers. The highest deviation between measured and simulated path powers was 2.8 dB and it occurred at the second weakest path. In NLOS the model was able to predict the dominant paths, diffracted or reflected. However, the tails of dominant paths, probably resulting from higher order reflections, were not identified well, because the used model implementation supported only for the first order reflections. The highest error was 2.4 dB on a diffracted path. In OLOS the main propagation mechanisms were reflection and scattering. Of course the shadowing of the LOS path was also considerable. Again, the dominant paths were identified with the maximum deviation of 2.5 dB, but few second order reflected paths were not modelled, due to the aforementioned reason. We want the emphasize that the map-based model itself contains higher order reflections, but the particular implementation in [31] did not. In the overall conclusion, the agreement between the map-based model outputs and the measurement results was found acceptable.

B. Outdoor

An outdoor measurement at 10.1 GHz frequency with 500 MHz bandwidth is reported in [32]. The environment was of an urban micro-cellular type, with building walls of concrete and partially covered by corrugated metallic sliding. The measurement device was a vector network analyzer. In both link ends a 5×5 virtual array was used, in Tx pointing in Rx direction and in Rx pointing in four different azimuth directions (composing the sides of a virtual cube). Eight LOS location of Rx and eight NLOS locations were measured. In the latter case, the Rx was behind a corner of a building. Map of the measurement environment was defined for the model. The bi-directional azimuth and elevation angles, delays, and powers of multipath components were estimated using ESPRIT algorithm. The dynamic range of 30 and 20 dB in LOS and NLOS cases, respectively, was considered.

In Rx locations with LOS the modelled direct and ground reflected paths matched well with the measured. The reflected and scattered paths were also predicted with some decibels of deviation to the measured. The model indicates diffraction as the dominant propagation effect in NLOS. However, according to the measurement this was the case only in part of Rx locations. However, in a sub-set of NLOS Rx location, the higher order reflections and scattering from metallic structures were dominant. Diffuse scattering did not show very precise alignment, which may be explained by the specific wall coating while all wall materials were assumed to be concrete in the map-based model. As a summary, the model was able to predict the most significant paths in the LOS case, but succeeded only partially in the NLOS locations.

C. Vehicle-to-Vehicle

We are validating the proposed model against a vehicle-to-vehicle (V2V) path loss measurement at 5.25 GHz in the city centre of Oulu. The measurement device was Propsound channel sounder. Omni-directional Tx and Rx antennas were mounted on top of cars at heights 1.6 and 2.5 m, respectively. Cars were driving along streets, both in opposite directions and the same direction. In the sub-set of data considered here the LOS was kept between Tx and Rx cars. However, high vehicles were occasionally present obstructing the actual LOS path temporarily. Oulu city centre has Manhattan type of regular street layout with four to six storey buildings. Streets

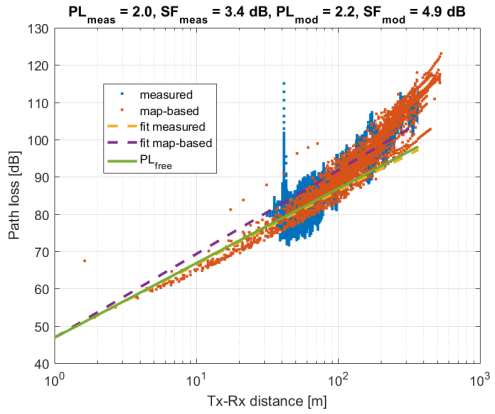

Fig. 6. Measured and modelled path losses at 5.25 GHz in vehicle-to-vehicle channels.

have mainly one lane per direction, thus having mostly two lanes per street. The measurement campaign is described in detail in [33].

With the map-based model we generated radio channel data for all 16032 links between 32 Tx locations and 501 Rx locations, randomly dropped on the streets of the city layout (Madrid grid) depicted in Fig. 8 (left). Then we took the sub-set with LOS condition and predicted the path loss. The same definition of LOS condition was used as in the measurement, i.e. both cars are on the same street. Antenna heights were equal to the measurement and the height of random objects was set to 1.5 m. It is noted that we did not intentionally use the layout of Oulu city centre in the simulation, because the purpose of the proposed model is not to generate strictly site-specific radio channel conditions. In this case, however, the environments were similar (straight streets with 90° intersections). Only with taller buildings and slightly wider streets of Madrid grid.

Both measured and simulated path loss samples are shown in Fig. 6. The spike on measurement data at 40 m distance is caused by a high bus blocking the LOS path for the duration of many measurement cycles. In addition, the figure contains log-linear path loss functions that are fitted to the data by minimizing the rms error. In fitting, the line is anchored to a reference point, which is the free space loss at 1 m Tx–Rx distance. Measured and predicted path loss exponents are 2.0 and 2.2, and shadowing standard deviations 3.4 dB and 4.9 dB, respectively. Predicted path loss samples agree well with the measured ones and the resulting path loss exponents are both close to the free space loss, which is expectable in LOS condition. Shadowing has 1.5 dB higher variation in the predicted case. This more statistical and less site-specific analysis validates that the model is capable of reconstructing channel conditions with realistic path losses in the specified V2V case. This validation is briefly introduced also in [10].

V. Computer Simulations

With simulations our intention is to investigate outputs and characteristics of the map-based model and also to compare them to outputs of a corresponding GSCM. Among other evaluations a comparison is done for the MU-MIMO sum rate capacity. MU-MIMO with massive MIMO antenna arrays is seen as an enabling technology to improve spectral efficiency of 5G networks [34]. We have chosen sum rate capacity as an evaluation metric, because we expect that it can give insight to the spatial structure of a multi-link radio channel and to reveal possible differences between the modelling principles.

A. Simulation Settings

The modelled environment is urban micro-cellular "Madrid grid" and the centre frequency is 2 GHz. A Matlab implementation was used to generate radio channel realizations for the map-based model. The "Madrid grid" is an irregular 3D city layout, illustrated in Figures 7, 8 and specified in more detail in [4]. Heights of rectangular building vary between 28 and 52.5 metres and street widths vary between 18 and 30 metres. The environment layout is depicted in Fig. 8 with a single BS location, denoted by a red triangle and three groups of randomly located UEs on different street segments, 100 UEs in each group, denoted by circles (hollow for LOS and solid for NLOS). UEs are categorized by their location to groups named 1) *LOS* on the same street with the BS, 2) *NLOS* on a *perpendicular* street South from the BS, and 3) *NLOS* on a *parallel* street East from the BS. The heights of the BS and the UEs are 7 and 1.5 metres, respectively. In the map-based model there are random objects present with density of $0.05/\mathrm{m}^2$. The model parameter reflected to scattered power ratio $\beta = 0.5$ and the object absorption coefficient $\alpha = 0$. In the implementation used for simulations the over roof-top propagation is considered only if either of the link ends is above roof-top level [20]. Thus, in the simulated case no propagation paths were modelled over buildings.

Fig. 8 has colour coding on UE locations indicating the receiver signal to noise ratio (SNR). It is worth noticing, that the the BS has different transmitting (Tx) power for different UE groups, namely 23 dBm for LOS UEs and 40 dBm for NLOS UEs. In total 111 independent samples of the channel transfer function are generated for each BS-UE link, utilizing the procedure described in section III, with the virtual motion principle.

GSCM channel samples were generated for a modified IMT-Advanced UMi (urban micro) model [13] with Keysight's Geometric Channel Modelling Tool. The original IMT-Advanced model is two dimensional only, but for this case it is extended to 3D by taking elevation parameters from [35]. The same BS and UE coordinates as in Fig. 8 are specified for the IMT-Advanced UMi model in order to aligning the LOS directions and link distances between the two models. The path loss model of Manhattan layout is used for the *perpendicular* UE group, while the hexagonal layout and LOS path loss models are used for the *parallel* and LOS groups, respectively [13]. Again 111 channel samples per link are generated.

BS antenna is a planar array with eight vertical columns, four horizontal rows and the inter-element spacing, in vertical and horizontal dimensions, of half wavelengths. Each array element is a dual polarized theoretical patch element with $\pm 45^\circ$ slanted linear polarizations. The total number of BS

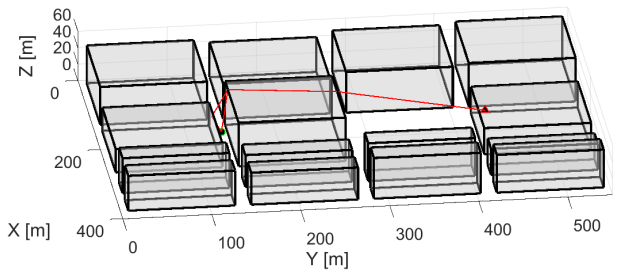

Fig. 7. 3D view of the Madrid grid with an example path (red line) diffracted over the roof top.

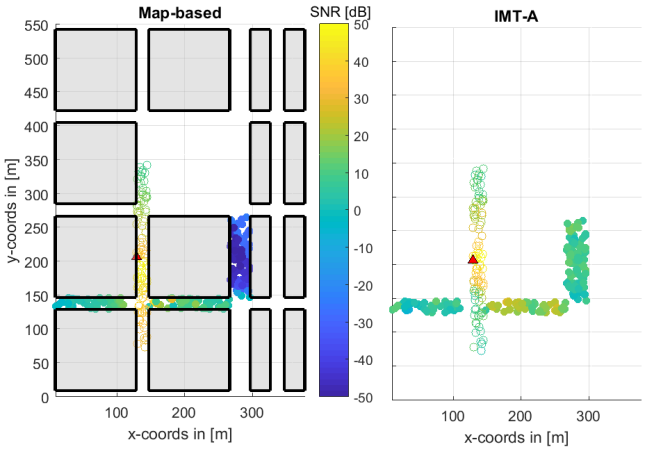

Fig. 8. Dense urban layout with BS location and 300 UE locations. SNR in UE locations with the map-based model is on left and with IMT-Advanced model on right.

antenna ports is 64 and the broad side of BS array is pointing East. UE antennas have two co-located $\pm 45^\circ$ slanted isotropic elements.

The output of channel generation procedures with both the map-based and GSCM models is two-fold. Firstly, propagation parameter sets for each 300 links (BS-UE location pairs), containing, e.g., path numbers, path/cluster directions, path delays, etc. Secondly, the output is 64×2 MIMO channel transfer matrices $\mathbf{H}(t, f)$ for each link and for 111 discrete values of t.

B. Simulation Results

1) Propagation parameter statistics: As a first comparison a set of statistical parameters are calculated from the propagation parameters of the two models. The parameters and their values are listed in Table I, where the symbols and acronyms are as follows: K number of paths, DS delay spread, ASA spread of arrival (UE) azimuth angles, ASD spread of departure (BS) azimuth angles, ESA spread of arrival elevation angles, ESD spread of departure elevation angles, KF Ricean K-factor, and sub-scripts μ & σ denote the mean & the standard deviation, respectively. Definitions and procedures to estimate the statistical parameters are given, e.g., in [12, Part II]. Only paths within 30 dB dynamic range are considered in this evaluation. The table has separate columns for the three UE groups with the map-based model. With the GSCM model the groups *perpendicular* and *parallel* are combined, because GSCM doesn't differentiate these cases.

We can observe from Table I that rather different statistics are realized in different NLOS configurations with the map-based model. Comparing delay and azimuth spreads in *perpendicular* and *parallel* cases the latter has significantly higher values. In the former case there is only one major propagation pathway, while in the latter there are two, as can be interpreted from Fig. 8. Typically in GSCMs power distributions are modelled by single distributions, with fixed distribution shapes (functions). However, this kind of urban canyon environment cannot be modelled well by any symmetric angular power distribution function. The angular power distribution at BS side is illustrated in Fig. 9, where propagation paths of all UEs are plotted on different UE categories and with the both models. The per links channel gains are normalized in the figure, i.e. the path loss is neglected.

When comparing the mean spread values of the map-based model to the corresponding parameters of GSCM we can observe they are clearly smaller, except in the *parallel* case. The multi-path richness of the GSCM is higher, as shown in Fig. 9. We can deduce this from the modelling principle, though it is not that easily readable from the spread parameters, and from capacity results of the next sub-section V-B2. For example the mean ASD in the *parallel* case is higher compared to GSCM NLOS case, even though the distribution of AoDs is condensed to the street openings. This observation is aligned with [36] in where is discussed that rms spread as a single number metric is not capable of capturing the detailed structures of power dispersions.

The model types have significant difference also on the elevation spreads, especially on ESD. With the map-based model in NLOS cases the propagation paths are practically not separable in the elevation domain by the BS. The difference between the two model types is obvious in Fig. 9, especially in NLOS cases. A global elevation spread is calculated over all paths of all UEs in a group with normalized path gains (neglecting path loss). These spread values are similar in LOS with the two models, approximately 11 deg. However, in NLOS cases the difference is substantial. Global elevation spreads are more than order of magnitude larger with the GSCM (6.7 deg) compared to the map-based ($0.4 - 0.58$ deg).

Similarly to our findings, differences between characteristics of different street categories are observed in [37], with ray tracing simulations verified by measurements in an urban layout. The investigated parameter was path loss, which is often modelled as a distance dependent parameter. Found path loss values were rather consistent for UE locations on the same streets and the fitted standard deviations of shadow fading were low. On the other hand, for UE locations on different streets the path loss exponents had high variability. If all simulated path losses were taken together and a regression line was fitted, the remaining standard deviation (modelling shadow fading) would have been very high. Our findings induce a conclusion that in addition to the path loss, as was shown in [37], also the power angular distribution has a strong dependency on the street categorization and orientation with respect to the Tx/Rx

TABLE I
STATISTICS OF PARAMETERS.

		Map-based			GSCM	
Parameter	unit	LOS	Perp	Paral	LOS	NLOS
K_μ	-	4.7	13.0	15.6	11.1	11.8
K_σ	-	1.7	3.3	8.0	1.9	0.5
DS_μ	ns	7.9	44.5	149.2	99.5	175.3
DS_σ	ns	10.8	15.5	111.8	108.2	215.5
ASA_μ	deg	5.9	8.6	38.1	32.3	64.4
ASA_σ	deg	4.4	7.6	24.0	17.9	16.1
ASD_μ	deg	7.1	7.8	31.9	17.2	26.7
ASD_σ	deg	8.3	2.3	26.6	14.6	11.6
ESA_μ	deg	3.5	0.2	0.1	5.0	11.0
ESA_σ	deg	5.7	0.1	0.1	3.8	10.6
ESD_μ	deg	0.8	0.2	0.1	2.5	5.4
ESD_σ	deg	1.0	0.1	0.1	1.4	3.1
KF_μ	dB	7.5	-	-	8.4	-
KF_σ	dB	5.4	-	-	5.4	-

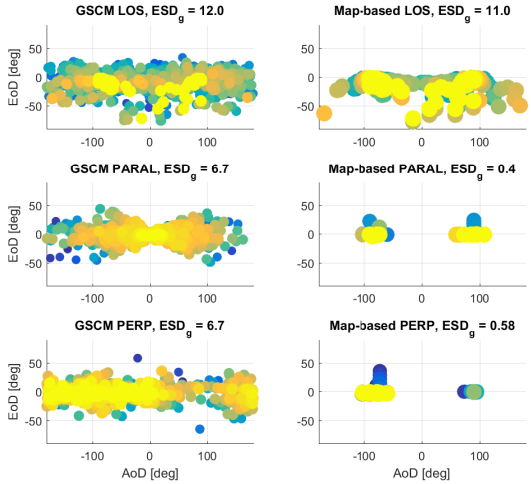

Fig. 9. Angular power distributions at the BS side. From top left to bottom right the figures are: GSCM LOS, GSCM paral, GSCM perp, map-based LOS, map-based paral, map-based perp. Colour and size of markers indicate the path gain.

locations.

2) Sum rate capacity: The second evaluation is done on the sum rate capacity of MU-MIMO communications, where a BS may serve a number of UEs utilizing the same time/frequency resources of the channel. The multiple access is enabled by spatio-polarimetric separation of UEs. In the simulated MU-MIMO transmission a linear precoding is used. No scheduling is performed to select the UEs to be served, instead sub-sets of UEs are drawn randomly.

At first a sub-set σ of ξ UEs is picked. The channel transfer matrix $\mathbf{H}_\sigma(t,f)$ for a sub-set σ is $64\times 2\xi$ matrix, composed by stacking per link transfer matrices in the column dimension. Then linear pre-coding vectors are determined for each UE of the sub-set by the zero forcing method [38], which is a sub-optimal linear pre-coding method and aims to achieve zero interference between users. The matrix composed of pre-coding vectors is calculated with the well known Moore-Penrose pseudo-inverse as follows

$$\mathbf{W}(t,f) = \mathbf{H}_\sigma^H(t,f)\left(\mathbf{H}_\sigma(t,f)\mathbf{H}_\sigma^H(t,f)\right)^{-1} \quad (18)$$

after which the rows $\mathbf{w}_k(t,f)$ of $\mathbf{W}(t,f)$ are normalized. The sum rate capacity is calculated as [38]

$$C(t,f) = \sum_{k=1}^{\xi} \log_2\left(1+\frac{\gamma}{\xi}\left|\mathbf{w}_k(t,f)\mathbf{h}_k(t,f)\right|^2\right), \quad (19)$$

where in the *fixed SNR* case the signal-to-noise ratio $\gamma = 20$ dB and $\mathbf{h}_k(t)$ are column vectors of $\mathbf{H}_\sigma(t,f)$. Finally, the average sum rate capacity for the sub-set σ is obtained from $C(t,f)$ by taking mean over t and f.

In the fixed SNR case the channel matrix is normalized to have the average channel gain over links, time, and frequency, equal to one, i.e. such that

$$\frac{1}{TF\,64\cdot 2\xi}\sum_t\sum_f \left\|\mathbf{H}_\sigma(t,f)\right\|_F^2 = 1, \quad (20)$$

where T and F are the numbers of discrete time and frequency samples, respectively. This case doesn't contain path loss or shadowing effects, but it is expected to indicate the differences in multi-path richness and degrees of freedom offered by the channel models. The second alternative to evaluate the sum rate capacity is the *fixed Tx power* case, which takes also the differences in path loss modelling in consideration. In this case the channel gains are not normalized, but a fixed Tx power of 23 dBm (LOS links) and 40 dBm (NLOS links) for 100 MHz bandwidth is assumed. The SNR term for eq. (19) is ratio of the Tx power and the thermal noise power on the bandwidth.

In the sum rate capacity simulation we pick randomly ξ UEs from 100 UEs of each location category. The considered capacity is the mean of instantaneous $C(t,f)$ over time and frequency, where $T = 111$ and $F = 100$ in the simulation. The random picking of sub-sets is done 1000 times, resulting to 1000 mean sum rate capacity values per UE location category. First we evaluate the impact of ξ on the sum rate capacity. Fig. 10 and 11 show medians of mean capacity values with $\xi = 2,\ldots,32$ in the *fixed SNR* and *fixed transmit power* cases, respectively. The highest median capacities are collected in Table II. The results indicate, among other things, how many UEs on average can be spatially separated with the given radio channel conditions. The map-based model predicts far more conservative sum rate capacities with most ξ values and the overall difference between the compared channel models is substantial.

The median capacities are higher in LOS cases and lower in NLOS cases, when comparing the *fixed transmit power* and *fixed SNR* (20 dB) simulations. This is expected observing the SNRs plotted in Fig. 8. With the map-based model the LOS channel supports for larger sub-set sizes and offers higher capacity than the NLOS condition. With IMT-A model the highest sum rate capacities are achieved in NLOS condition, but larger ξ values are supported by the LOS condition. Sub-set size $\xi = 32$, i.e. the condition when the number of Rx antennas equals the number of Tx antennas, is the upper limit for the zero forcing precoding.

TABLE II
SUM RATE CAPACITIES.

	Highest median sum rate capacity [bps/Hz]		Probability of sum rate capacity 30 bps/Hz or higher (ξ=10/2) [%]	
Model	Fixed SNR	Fixed P_{tx}	Fixed SNR	Fixed P_{tx}
LOS map-based	36.3	103.2	58	98
LOS IMT-A UMi	42.9	141.1	64	100
perp map-based	16.2	18.2	3	3
perp IMT-A UMi	70.2	12.6	49	40
paral map-based	12.1	0	3	0
paral IMT-A UMi	90.3	5.4	99	6

Further, from the figures we can read the sub-set sizes ξ providing highest capacities in different scenarios. For example in the *fixed SNR* case $\xi = 10$ is optimal with the IMT-A NLOS, while $\xi = 2$ offers the highest capacity with the map-based NLOS UEs. In LOS condition the best median capacity is achieved approximately when $\xi \in [10, 20]$. This motivated the selection of sub-set sizes ξ for evaluation of distributions of the sum rate capacities in Fig. 12 and 13. There the sum rate capacity for the group of 100 LOS condition UEs is calculated in sub-sets of $\xi = 10$, 15, and 20 UEs. Similarly for the two NLOS groups the sub-set sizes are $\xi = 2$, 3, and 4.

Empirical cumulative distribution functions (CDF) of the sum rate capacity with *fixed SNR* are plotted in Fig. 12. From the simulation results we can make several findings. In all evaluated cases GSCM results to higher sum rate capacity compared to the map-based model, however, in LOS condition with $\xi = 10$ the capacities are rather equal. I.e. GSCM gives more optimistic impression on the MU-MIMO potential in urban environment. With the map-based model LOS condition almost always outperforms NLOS condition, even in this fixed SNR case, where path loss is not considered. With GSCM the NLOS condition gets more favourable than LOS when increasing the UE sub-set size ξ, except in the highest 10% portion of the distribution. The observations are well explained by the city layout in Fig. 8 and the angular power distribution in 9, where the signal propagates to NLOS UEs only via few, one or two, street canyon pathways. The layout affects the map-based model, while IMT-A UMi model is mostly insensitive to the similarity of UEs propagation environments. Obviously GSCM model offers substantially more spatially separable channels compared to the map-based model. Namely the sum rate capacity increases when increasing ξ with the former, but decreases with the latter.

One explaining factor is the higher spread of elevation angles in GSCM NLOS cases, as illustrated in Fig. 9. In these cases, the BS is still able to separate UEs in the elevation domain, while with the map-based model NLOS cases the elevation domain is practically useless. This means that the vertical dimension of the BS array was mostly redundant for the NLOS users.

Similarly CDF curves for the *fixed Tx power* case are shown in Fig. 13. The overall behaviour is similar to the fixed SNR case, except that capacities with LOS UEs clearly outperform NLOS on both models, which is expected due to stronger path loss in the latter condition. Moreover, the LOS

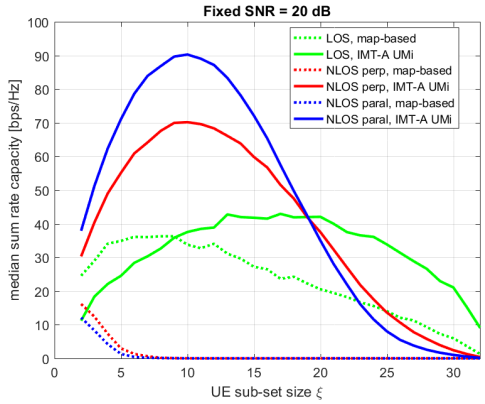

Fig. 10. Median sum rate capacities in fixed SNR case, as a function of UE sub-set size ξ.

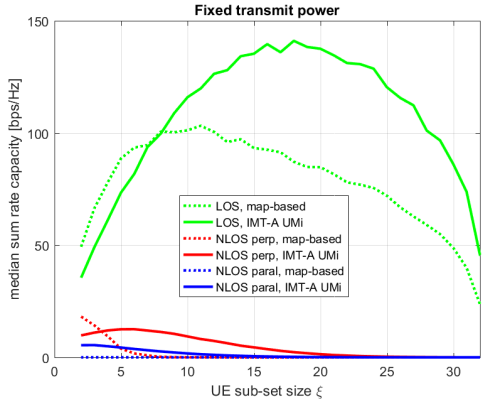

Fig. 11. Median sum rate capacities in fixed transmit power case, as a function of UE sub-set size ξ.

performances are better compared with the *fixed SNR* case, as can be expected observing the SNR values plotted in Fig. 8. With the map-based model in *NLOS parallel* street UE group the sum rate capacity is practically zero, even with 2 UEs sub-set size. The path loss is too high to the street behind a building block. We have listed in Table II the probabilities of achieving sum rate capacity 30 bps/Hz or higher from CDFs of Fig. 12 (top) and 13 (top) for numerical comparison. The table provides probabilities for both the *fixed SNR* and the *fixed Tx power* cases. In LOS condition the probability difference between two models is two and six percent units indicating a fair alignment. In NLOS condition, as discussed previously, the deviation is significant, being 46 and 37 percent units in the *perpendicular* case, and 96 and 6 percent units in the *parallel* case.

VI. SUMMARY

The coming 5G wireless communication system is going to have many new features, such as massive MIMO, ultra dense deployment, operation on higher frequency bands, and device-to-device links. We have discussed a number of requirements set to channel models by the new features. Among the most important ones is the seamless and realistic modelling across

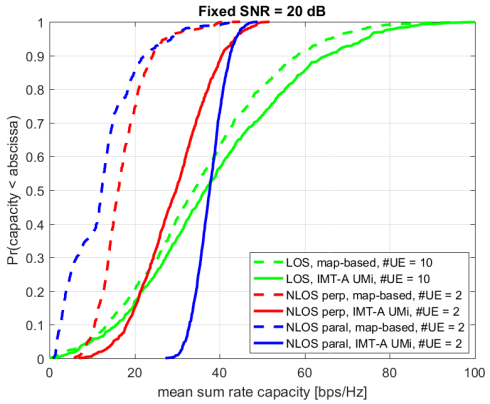

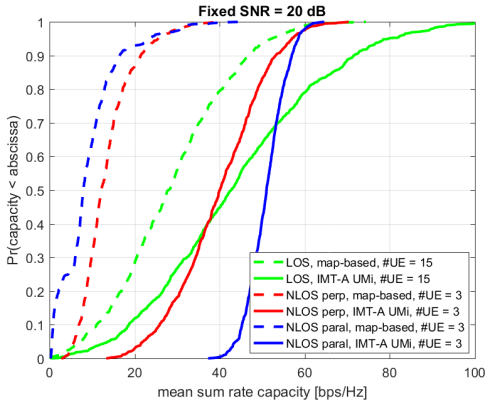

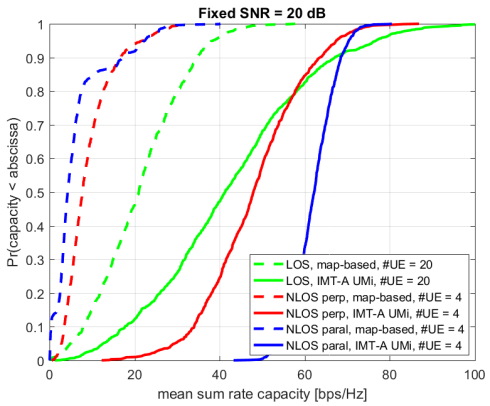

Fig. 12. CDFs of sum rate capacities with fixed SNR for $\xi = 10/2$, 15/3, and 20/4 UEs per sub-set.

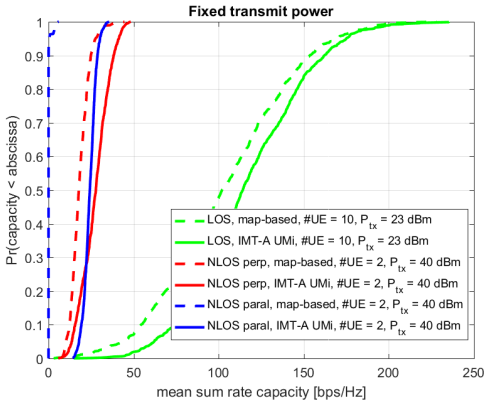

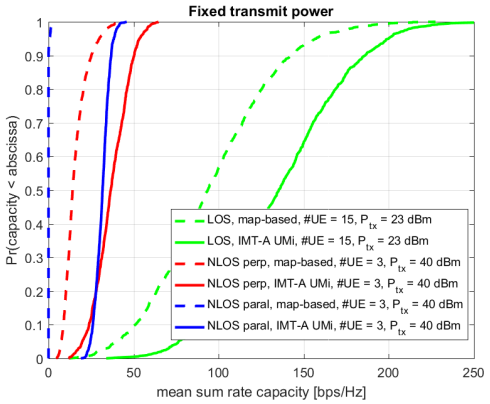

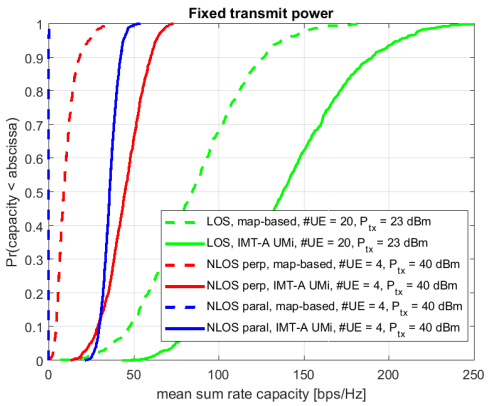

Fig. 13. CDFs of sum rate capacities with fixed Tx power for $\xi = 10/2$, 15/3, and 20/4 UEs per sub-set.

wide frequency range and the spatially consistent modelling of numerous radio links. We have introduced a channel model that is capable of addressing the identified requirements.

The map-based model is described at level of details sufficient for obtaining understanding of all its components and its overall functionality. The coordinate based description of the modelled environment with a stochastic element of random objects together with the deterministic ray tracing principle is the key to achieving consistent but versatile radio channel realizations as the model output.

In the simulation part we have generated and compared outputs of the proposed model with a modified IMT-Advanced UMi [13] model that belongs to the GSCM family. We did a few findings on the distributions of the second moments of angular and delay parameters. Firstly, the map-based model has highly different second moments on the two categories of NLOS UE locations. It indicates that the second moments are not a perfect metric for describing a propagation environment. Secondly, the second moments are notably smaller in the LOS and in the *perpendicular* street cases of the map-based model compared with the corresponding GSCM cases. Further, we observed a fundamental difference in the NLOS directional power distribution on the BS side between the two models. The same fundamental difference is shown also by the simulated MU-MIMO sum rate capacities. GSCM offers substantially more optimistic picture of the MU-MIMO potential. We do not have comparable measurement results on MU-MIMO performance in urban outdoor environments. However, based

on the simulation results we claim that the GSCM seriously over-estimates the capacity of MU-MIMO and the spatial separability of UEs by massive MIMO BS arrays in urban street canyon environments, especially in NLOS condition.

Future investigation are needed at least for determining frequency dependent diffuse/specular power ratio. Currently it can be done with surface roughness assumptions, but the roughness model is not well suited for this wide frequency range. The larger portion of diffuse power would result in a richer multi-path channel. Further studies could be done also on combining more stochastic elements to the proposed model, in order to define a hybrid model. One alternative is already introduced in [8], but other options could be studied.

ACKNOWLEDGMENT

The part of this research performed at University of Oulu has been supported by Finnish Funding Agency for Technology and Innovation (Tekes), Huawei Technologies, Nokia and Anite Telecoms/Keysight Technologies Finland Oy.

REFERENCES

[1] J. G. Andrews, S. Buzzi, W. Choi, S. V. Hanly, A. Lozano, A. C. K. Soong, and J. C. Zhang, "What will 5G be?" *IEEE Journal on Selected Areas in Communications*, vol. 32, no. 6, pp. 1065–1082, June 2014.

[2] A. Osseiran, J. F. Monserrat, P. Marsch, M. Dohler, and T. Nakamura, Eds., *5G Mobile and Wireless Communications Technology*. Cambridge University Press, July 2016.

[3] Aalto University, BUPT, CMCC, Nokia, NTT DOCOMO, New York University, Ericsson, Qualcomm, Huawei, Samsung Electronics, Intel, University of Bristol, KT Corporation, and University of Southern California, "White paper on 5G channel model for bands up to 100 GHz," v2.0, March 2016.

[4] L. Rachowski, P. Kyösti, K. Kusume, and T. Jämsä (editors), "METIS Channel Models, Deliverable 1.4 v.1.3," ICT-317669 METIS project, Tech. Rep., 2015.

[5] J. Medbo et al., "Channel modelling for the fifth generation mobile communications," in *The 8th European Conference on Antennas and Propagation (EuCAP 2014)*, April 2014, pp. 219–223.

[6] S. Jaeckel, M. Peter, K. Sakaguchi, W. Keusgen, and J. Medbo, "5G channel models in mm-Wave frequency bands," in *22th European Wireless Conference 2016 (EW)*, May 2016, pp. 1–6.

[7] M. K. Samimi and T. S. Rappaport, "3-D millimeter-Wave statistical channel model for 5G wireless system design," *IEEE Transactions on Microwave Theory and Techniques*, vol. 64, no. 7, pp. 2207–2225, July 2016.

[8] TR 38.900, "Channel model for frequency spectrum above 6 GHz," 3GPP, Tech. Rep. Rel 14, V2.0.0, June 2016.

[9] "Future spectrum requirements estimate for terrestrial IMT," ITU-R Report M.2290, Tech. Rep., December 2013.

[10] J. Medbo, P. Kyösti, K. Kusume, L. Raschkowski, K. Haneda, T. Jämsä, V. Nurmela, A. Roivainen, and J. Meinilä, "Radio propagation modeling for 5G mobile and wireless communications," *IEEE Communications Magazine*, vol. 54, no. 6, pp. 144–151, June 2016.

[11] J. F. Monserrat and M. Fallgren (editors), "Simulation guidelines, Deliverable 6.1 v1," ICT-317669 METIS project, Tech. Rep., 2013.

[12] P. Kyösti et al., "IST-4-027756 WINNER II Deliverable 1.1.2. v.1.2, WINNER II Channel Models," IST-WINNER2, Tech. Rep., 2007.

[13] "Guidelines for evaluation of radio interface technologies for IMT-Advanced, ITU-R Report M.2135-1," ITU-R, Tech. Rep., December 2009.

[14] TR 36.873, "Study on 3D channel model for LTE," 3GPP, Tech. Rep. V12.2.0, June 2015.

[15] V. Degli-Esposti, D. Guiducci, A. de'Marsi, P. Azzi, and F. Fuschini, "An advanced field prediction model including diffuse scattering," *IEEE Transactions on Antennas and Propagation*, vol. 52, no. 7, pp. 1717–1728, July 2004.

[16] X. Gao, O. Edfors, F. Rusek, and F. Tufvesson, "Massive MIMO performance evaluation based on measured propagation data," *IEEE Transactions on Wireless Communications*, vol. 14, no. 7, pp. 3899–3911, July 2015.

[17] A. Karttunen, J. Järveläinen, A. Khatun, and K. Haneda, "Radio propagation measurements and WINNER II parameterization for a shopping mall at 60 GHz," in *IEEE 81st Vehicular Technology Conference (VTC Spring)*, May 2015, pp. 1–5.

[18] R1-163095, "Simulations of map-based hybrid channel model," 3GPP, Tech. Rep. TSG-RAN WG1 84bis, April 2016.

[19] S. Y. Seidel and T. S. Rappaport, "Site-specific propagation prediction for wireless in-building personal communication system design," *IEEE Transactions on Vehicular Technology*, vol. 43, no. 4, pp. 879–891, Nov 1994.

[20] K. R. Schaubach, N. J. Davis, and T. S. Rappaport, "A ray tracing method for predicting path loss and delay spread in microcellular environments," in *[1992 Proceedings] Vehicular Technology Society 42nd VTS Conference - Frontiers of Technology*, May 1992, pp. 932–935 vol.2.

[21] G. Liang and H. L. Bertoni, "A new approach to 3-D ray tracing for propagation prediction in cities," *IEEE Transactions on Antennas and Propagation*, vol. 46, no. 6, pp. 853–863, Jun 1998.

[22] J. E. Berg, "A recursive method for street microcell path loss calculations," in *Sixth IEEE International Symposium on Personal, Indoor and Mobile Radio Communications (PIMRC'95)*, vol. 1, Sep 1995, pp. 140–143.

[23] R. C. Jones, "A new calculus for the treatment of optical systems," *J. Opt. Soc. Am.*, vol. 31, no. 7, pp. 500–503, Jul 1941.

[24] R. Vaughan and J. B. Andersen, *Channels, Propagation and Antennas for Mobile Communications*. The IEE, London, UK, 2003.

[25] "Effects of building materials and structures on radiowave propagation above about 100 MHz," ITU-R Report P.2040-1, Tech. Rep., July 2015.

[26] R. G. Kouyoumjian and P. H. Pathak, "A uniform geometrical theory of diffraction for an edge in a perfectly conducting surface," *Proceedings of the IEEE*, vol. 62, no. 11, pp. 1448–1461, Nov 1974.

[27] R. Luebbers, "Finite conductivity uniform GTD versus knife edge diffraction in prediction of propagation path loss," *IEEE Transactions on Antennas and Propagation*, vol. 32, no. 1, pp. 70–76, Jan 1984.

[28] J. Medbo and F. Harrysson, "Channel modeling for the stationary UE scenario," in *7th European Conference on Antennas and Propagation (EuCAP 2013)*, April 2013, pp. 2811–2815.

[29] J. Walfisch and H. L. Bertoni, "A theoretical model of UHF propagation in urban environments," *IEEE Transactions on Antennas and Propagation*, vol. 36, no. 12, pp. 1788–1796, Dec 1988.

[30] G. L. Ramos, P. Kyösti, V. Hovinen, and M. Latva-aho, "Multiple-screen diffraction measurement at 10–18 GHz," *IEEE Antennas and Wireless Propagation Letters*, vol. 16, pp. 2002–2005, 2017.

[31] I. Carton, W. Fan, P. Kyösti, and G. F. Pedersen, "Validation of 5G METIS map-based channel model at mmWave bands in indoor scenarios," in *The 10th European Conference on Antennas and Propagation (EuCAP 2016)*, April 2016.

[32] A. Roivainen, P. Kyösti, V. Hovinen, C. Ferreira Dias, N. Tervo, M. Sonkki, G. Fraidenraich, and M. Latva-aho, "Validation of deterministic radio channel model by 10 GHz microcell measurements," in *European Wireless Workshops (EWW 2016)*, May 2016.

[33] A. Roivainen, P. Jayasinghe, J. Meinilä, V. Hovinen, and M. Latva-aho, "Vehicle-to-vehicle radio channel characterization in urban environment at 2.3 GHz and 5.25 GHz," in *2014 IEEE 25th Annual International Symposium on Personal, Indoor, and Mobile Radio Communication (PIMRC)*, Sept 2014, pp. 63–67.

[34] E. G. Larsson, O. Edfors, F. Tufvesson, and T. L. Marzetta, "Massive MIMO for next generation wireless systems," *IEEE Communications Magazine*, vol. 52, no. 2, pp. 186–195, February 2014.

[35] L. Hentilä, P. Kyösti, and J. Meinilä, "Elevation Extension for a Geometry based Radio Channel Model and its Influence on MIMO Antenna Correlation and Gain Imbalance," *in Proc. of the 5th European conference on antennas and propagation, (EuCAP 2011), Rome, Italy*, April 2011.

[36] N. Czink, X. Yin, H. Özcelik, M. Herdin, E. Bonek, and B. H. Fleury, "Cluster characteristics in a MIMO indoor propagation environment," *IEEE Transactions on Wireless Communications*, vol. 6, no. 4, pp. 1465–1475, April 2007.

[37] A. F. Molisch, A. Karttunen, S. Hur, J. Park, and J. Zhang, "Spatially consistent pathloss modeling for millimeter-wave channels in urban environments," in *2016 10th European Conference on Antennas and Propagation (EuCAP)*, April 2016, pp. 1–5.

[38] F. Kaltenberger, D. Gesbert, R. Knopp, and M. Kountouris, "Correlation and capacity of measured multi-user MIMO channels," in *2008 IEEE 19th International Symposium on Personal, Indoor and Mobile Radio Communications (PIMRC)*, August 2008, pp. 1–5.